Montel mirror based collimating analyzer system for high-pressure resonant inelastic X-ray scattering experiments

J.-K. Kim,[a,b,c] Diego Casa,[c] Xianrong Huang,[c] Thomas Gog,[c] B. J. Kim[a,b] and Jungho Kim[c]*

[a]Center for Artificial Low Dimensional Electronic Systems, Institute for Basic Science (IBS), Pohang 790-784, Republic of Korea, [b]Department of Physics, Pohang University of Science and Technology, Pohang 790-784, Republic of Korea, and [c]Advanced Photon Source, Argonne National Laboratory, Lemont, IL 60439, USA. *Correspondence e-mail: jhkim@anl.gov

Resonant inelastic X-ray scattering (RIXS) is increasingly playing a significant role in studying highly correlated systems, especially since it was proven capable of measuring low-energy magnetic excitations. However, despite high expectations for experimental evidence of novel magnetic phases at high pressure, unequivocal low-energy spectral signatures remain obscured by extrinsic scattering from material surrounding the sample in a diamond anvil cell (DAC): pressure media, Be gasket and the diamond anvils themselves. A scattered X-ray collimation based medium-energy resolution ($\sim$100 meV) analyzer system for a RIXS spectrometer at the Ir L_3-absorption edge has been designed and built to remediate these difficulties. Due to the confocal nature of the analyzer system, the majority of extrinsic scattering is rejected, yielding a clean low-energy excitation spectrum of an iridate Sr_2IrO_4 sample in a DAC cell. Furthermore, the energy resolution of different configurations of the collimating and analyzing optics are discussed.

1. Introduction

Resonant inelastic X-ray scattering (RIXS) is a photon-in/photon-out spectroscopic technique that provides invaluable information on the electronic and magnetic properties of complex materials (Ament *et al.*, 2011). After the momentous observation that RIXS can also detect single spin-flip excitations in cuprates (Ament *et al.*, 2009; Braicovich *et al.*, 2010), RIXS is considered as a unique alternative technique to inelastic neutron scattering for accessing elementary magnetic excitations and has been widely utilized to study various correlated systems (Chun *et al.*, 2015; Kim, Casa *et al.*, 2012; Kim, Said *et al.*, 2012).

Applying pressure is an effective way to tune interactions in a correlated system so that novel phases can be realized. In particular, superconducting and quantum spin liquid phases are expected to emerge upon applying pressure to certain iridate compounds (Haskel *et al.*, 2012, 2020; Majumder *et al.*, 2018; Yadav *et al.*, 2018). As such, novel phases can be identified by their particular spectral features corresponding to unique magnetic excitations; therefore, RIXS measurements at high pressure have been attempted on Sr_2IrO_4 and $Sr_3Ir_2O_7$ (Kim, 2016; Rossi *et al.*, 2019). However, it was instantly revealed that low-energy spectra are contaminated by extrinsic scattering from the high-pressure sample environment.

Indeed, when using a conventional RIXS spectrometer [using a diced spherical analyzer and a strip detector on a

Rowland circle (Shvyd'ko *et al.*, 2013)], this extrinsic scattering contamination is fundamentally inevitable. Although an attempt to use a post-sample clean-up slit alleviated the problem to some degree at the cost of signal reduction (Rossi *et al.*, 2019), it is still difficult to achieve a sufficiently small field of view (FOV) with a slit and, therefore, to avoid extrinsic scattering from a Be gasket at high pressures as its inner edge is squeezed increasingly closer to the sample. The slit needs to be located closer to the sample position for a smaller FOV, but a bulky diamond anvil cell (DAC) restricts the slit to a minimum distance from the sample.

Figure 1
(*a*) Schematic of a conventional energy-dispersive RIXS setup with a diced spherical analyzer A, a strip detector D, and sample S in a Rowland circle geometry (dashed). Extrinsic elastic scattering from point S′ ≠ S arrives at the detector at F′ ≠ F and is therefore counted at a different energy. (*b*) Schematic of a conventional RIXS setup with a bent spherical analyzer A. Scattered X-rays from S and S′ will be focused on different single points at F and F′ and therefore do not interfere with each other.

To circumvent this predicament, a scattered X-ray collimation (SXC) RIXS analyzer system was designed and built. Actual measurements in a DAC cell show that the confocal nature of the SXC optics can effectively reject extrinsic scattering and produce much cleaner spectra than a conventional setup based on a diced spherical analyzer, even in the extreme case where the pressure is increased to the point where the Be gasket actually touches the sample. Additionally, three different configurations of the SXC-RIXS spectrometer are tested and compared in terms of energy resolution.

2. Low-energy contamination and scattered X-ray collimation

A conventional RIXS spectrometer is shown schematically in Fig. 1(*a*). It consists of a diced spherical analyzer (A) and a strip detector (D) in a Rowland circle geometry that includes the sample (S) (Shvyd'ko *et al.*, 2013). The flat crystal dices of the analyzer disperse the scattered radiation from the sample, and the corresponding intensities are then assigned to different energies based on their position along the detector around the reference point F. An extrinsic source of elastic scattering S′ near S will disperse around a point F′ along the detector, therefore adding spectral intensity at different energies due to the displacement.

A bent analyzer, on the contrary, is rather insensitive to the presence of extrinsic scatterers because it focuses X-rays scattered from a single scatterer into a single focal point, as shown in Fig. 1(*a*). If an extrinsic scatterer (S′) were introduced, X-rays from the scatterer would be focused on another focal point (F′), which is newly defined by an extrinsic scatterer (S′) and analyzer (A) following the Rowland circle geometry. Thus, if

an area detector has enough resolution to resolve these two focal points (F and F′), then a RIXS spectrum of the target sample (S) would not be spoiled by extrinsic signals. This spatial resolution can be applied to direct tomography (Huotari *et al.*, 2011). However, the rather coarse resolution (few hundreds of meV) due to bending strain on the crystal makes it unsuitable for the measurements discussed here.

For a successful RIXS measurement under high pressure, here we explore a RIXS spectrometer based on flat-crystal optics that offers a high energy resolution and an important advantage regarding suppressing extrinsic signals, compared with the diced spherical analyzer system (Kim, 2016). The confocal property comes from its first optical element, a collimating laterally graded multilayer Montel mirror, shown schematically in Fig. 2(*a*). The Montel mirrors for RIXS and IXS spectrometers were designed and their performances were confirmed earlier (Kim *et al.*, 2016; Mundboth *et al.*, 2014). The relatively narrow reflectivity curve of the mirror [Fig. 2(*b*)] fundamentally rejects X-rays scattered from an extrinsic scattering source (S′). This concept can also be understood as a limited FOV of the Montel mirror at the sample position, which is the angular acceptance multiplied by the working distance, in this case 0.028° × 200 mm = 98 μm.
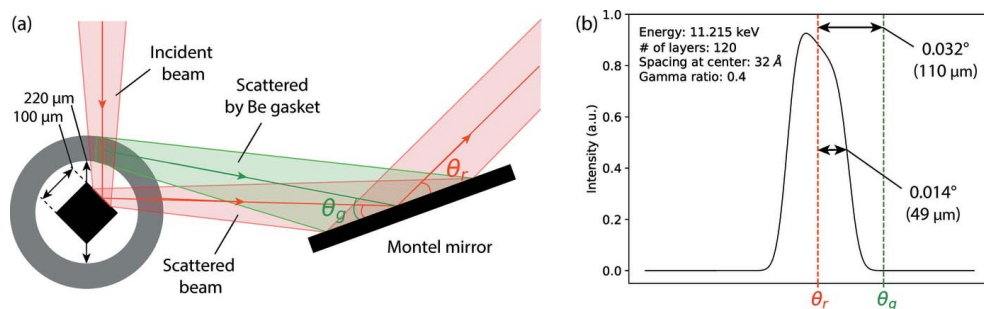

Figure 2
(*a*) Rejection of extrinsic signals from the Be gasket by a multilayer Montel mirror. Scattered X-rays from the sample (red) and extrinsic scattering from the Be gasket (green) arrive at the mirror surface at different incidence angles, θ_r and θ_g, respectively. Since the difference in incidence angles is larger than the width of the mirror rocking curve shown in (*b*), the contamination is rejected. The mirror's field of view (FOV) at the sample is 98 μm (FWHM of the rocking curve × 200 mm mirror–sample distance), clearly excluding rays emanating from the Be gasket.

Since the distance between the sample center and the Be gasket center, 110 µm, is larger than half of the Montel mirror's FOV, extrinsic signals from the Be gasket can be effectively rejected. We note that a collimating polycapillary optics and a flat analyzer crystal have been used for a few-eV-resolution high-pressure emission spectroscopy to collect the signal only from a small volume at its focus (Heald *et al.*, 2012) and also for a RIXS or IXS spectrometer for exceptionally high resolutions (Kim *et al.*, 2018; Shvyd'ko *et al.*, 2014).

3. Experimental

Fig. 3 introduces two configurations of the SXC-RIXS spectrometers for the experiments. In the configuration in Fig. 3(*a*), a crystal (C), asymmetrically (*b* = −0.0642) cut Si(111), is used to further collimate the X-rays exiting the Montel mirror (M). Detailed information on the Montel mirror can be found in a previous study (Kim *et al.*, 2016). Then, the symmetric flat analyzer crystal (A) selects the energies of the collimated X-rays. Fig. 3(*b*) describes a one-step collimating configuration of SXC-RIXS consisting of the Montel mirror (M) and a flat analyzer crystal (A). These configurations of SXC-RIXS spectrometers in Figs. 3(*a*) and 3(*b*) are referred to as the 'MCA' and 'MA' configurations, respectively.

The experiments were organized into two steps. First, RIXS spectra of an Sr_2IrO_4 single crystal in a DAC were obtained by a conventional-type spectrometer, such as shown in Fig. 1 which uses a diced spherical Si(844) analyzer on a 2 m arm. These were compared with the spectra measured by both MCA and MA setups with a symmetric Si(844) flat crystal analyzer to demonstrate and quantify the extrinsic scattering rejection capabilities of the SXC system. Afterwards, the confocal performance of the MA configuration was once more tested in the extreme case where the inner edge of the Be gasket touches the sample at high pressures (6.8 and 15.6 GPa).

Second, three different SXC-RIXS configurations are compared in terms of energy resolution using 3M Magic Scotch tape as an elastic reference scatterer. MCA/MA configurations with a flat Si(844) analyzer and an MA configuration with a flat sapphire(078) analyzer were tested. Experimentally obtained energy resolutions are then compared with the calculated ones.

The sample environment is shown schematically in Figs. 2(*a*) and 3(*c*). A pair of 0.25-carat brilliant-cut diamond anvils with 400 µm culets were fixed at the seats of a Mao-type symmetric pressure cell, which has four windows with ∼30° opening (Li *et al.*, 2018). A piece of Sr_2IrO_4 single crystal with *c*-axis oriented in the lateral plane was prepared by a focused ion beam (FIB) technique to a 100 µm × 100 µm lateral size with a thickness of 20 µm and was placed inside a 220 µm-diameter hole of a Be gasket along with ruby chips as a pressure reference. After closing the cell, Ne gas was loaded into the cell with a base pressure of 1.2 GPa. A *c*-axis Bragg peak was measured but the sample orientation was not fully determined in this study. The pressure was measured and controlled by an *in situ* membrane-driven and ruby-measurement system. During the experiment, two other pressures (6.8 GPa, 15.6 GPa) were reached besides the base pressure.

Measurements were performed at the 27-ID beamline at the Advanced Photon Source, where a diamond (111) high-heat-load monochromator and a four-bounce asymmetric Si(400) medium-resolution monochromator produced an X-ray beam at 11.215 keV with 70 meV bandpass (Shvyd'ko *et al.*, 2013). The beam was focused on 54 µm (H) × 16 µm (V) onto the sample using a KB mirror pair.

4. Result and discussion

4.1. Performance of Montel mirror and flat crystals

Fig. 4(*a*) shows RIXS spectra measured by three different spectrometers, demonstrating that SXC-RIXS spectrometers effectively reduce extrinsic signals from the sample environment, which contaminate the low-energy part of the spectrum measured using a diced spherical analyzer. It can be more clearly seen by fitting the spectra using known peaks at low-energy RIXS spectra of Sr_2IrO_4 (Kim, Casa *et al.*, 2012), as exhibited in Figs. 4(*c*) and 4(*d*). The RIXS spectrum taken by the MCA spectrometer in Fig. 4(*c*) is well fitted by three Gaussian-line-shaped peaks, which correspond to
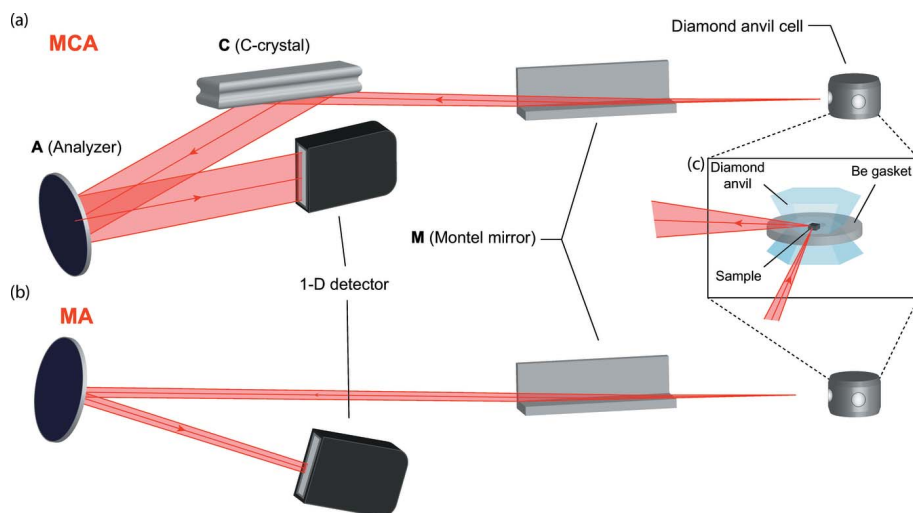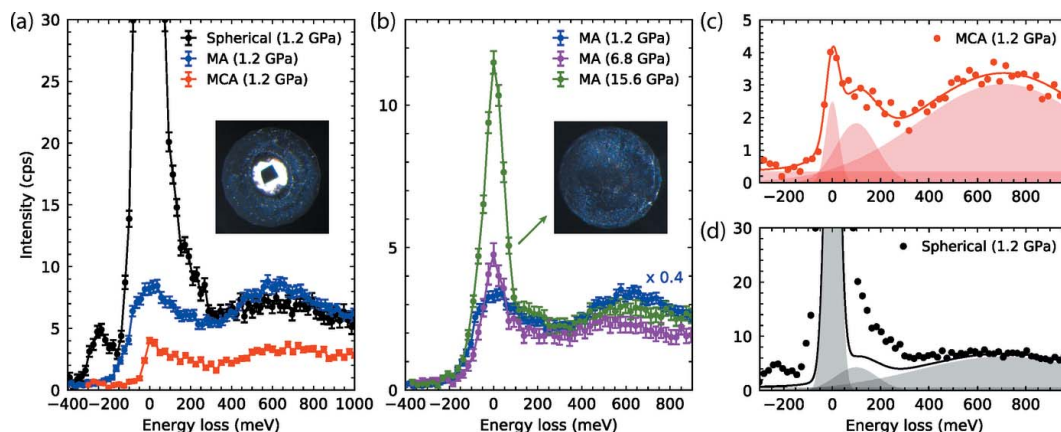

Figure 3
(*a*) SXC-RIXS spectrometer in the 'MCA' configuration, consisting of a collimating mirror M (laterally graded Ru/C multilayer Montel mirror), a collimating crystal C [asymmetrically cut Si (111)], and the analyzer A [symmetrically cut Si (844) or sapphire (078) crystal]. The 1D strip detector (MYTHEN) collects photons reflected by the analyzer A. (*b*) One-step collimating configuration 'MA' that does not include a C-crystal. (*c*) The diamond anvil cell high-pressure sample environment. A sample is contained in a space surrounded by diamond anvils and a Be gasket with Ne gas as a pressure medium and ruby chips for pressure monitoring. The X-rays pass through the Be gasket, which is relatively transparent to X-rays.

Figure 4
(a) Measured RIXS spectra with different spectrometers at the same pressure (1.2 GPa). The inset shows that the sample and its surroundings at the pressure. The spectrometer with a diced spherical analyzer gives huge extrinsic signals around the elastic point, whereas the SXC-RIXS spectrometers do not. (b) Measured RIXS spectra using the SXC-RIXS spectrometer with different pressures. As the inset shows, at 15.6 GPa, the Be gasket has collapsed and the sample can no longer be seen. (c) The same RIXS spectrum taken by an MCA in (a), which is fitted using Gaussian line shapes. The spectrum is well fitted by three peaks, which correspond to an elastic peak, magnon, and dd-excitation. (d) The same RIXS spectrum taken by a spherical analyzer in (a), which is plotted with the same Gaussian functions in (c). This spectrum cannot be well fitted since it contains lots of extrinsic signals from other than the sample.

an elastic line, magnon, and dd-excitation from low energy loss and, also, magnon and dd-excitations are located at the correct energies with proper widths. However, the RIXS spectrum taken by the conventional RIXS spectrometer with a spherical analyzer cannot be fully reproduced with those three peaks, showing a discrepancy between the line made by the three peaks (solid black line) and the actual spectrum (black dots), especially around the zero energy-loss.

Note that the count rate of the MA configuration is comparable with that of the conventional spectrometer using a diced spherical analyzer; the intensities around 600 meV (dd-excitation) in Fig. 4(a) are similar for both setups. Since the solid angle acceptance of scattered X-rays was kept constant by adjusting the mask size of the diced spherical analyzer, the intensities shown in Fig. 4(a) directly correspond to the efficiencies of the spectrometers.

The inset of Fig. 4(b) shows the sample environment at 15.6 GPa where the Be gasket collapses to contact the sample. As a collapsed Be gasket invades the FOV of the mirror at higher pressure, elastic signals increase upon applying higher pressures. Nevertheless, the SXC-RIXS spectrometer still works well and gives a clean low-energy excitation spectrum even in this extreme sample environment.

4.2. Comparing performances of the three different configurations

Figs. 5(a) and 5(b) show the measured and calculated incident-energy-dependence curves of three different SXC-RIXS spectrometers, and their resolutions and throughputs are tabulated in Table 1 (the calculation method is described in Appendix A). In the experimental results, the MCA setup with a Si(844) analyzer and the MA setup with a sapphire(078) analyzer have better energy resolutions than that of the MA setup with the Si(844) analyzer. Although the same kind of calculation greatly reproduced the measured resolutions of a

SXC-RIXS spectrometer in the previous study (Kim *et al.*, 2018), in our current case there is one major difference with the calculation: energy resolutions of the MA configurations are notably sharper than that calculated. This discrepancy could come from the multi-bounce monochromator used in this experiment, which consists of asymmetric crystals.

A multi-bounce monochromator consisting of asymmetric crystals is known to produce a vertically energy-dispersed beam spot at the sample position (Huang *et al.*, 2012), while the calculation here assumes no spatial energy dispersion. Therefore, when using a multi-bounce asymmetric monochromator, the Montel mirror emittance is correspondingly dispersed in the energy–angle space due to the finite beam size, which in turn results in a reduced width when rocking an analyzer crystal, which has a narrower acceptance than the divergence of the Montel mirror (the detailed explanation is given in Appendix B). These dispersion effects are not significant when using a C crystal since it collimates the mirror emittance to fit the analyzer crystal acceptance by design or trivially when using a symmetric channel-cut monochromator. Additionally, this dispersion effect also produces Lorentzian-like line shapes of the resolution curves for MA setups.

Throughputs are estimated by the integrated intensities under the curves, and used to compare the efficiency of each setup. In Table 1 it is seen that the relative throughput of two MA setups is reasonably explained by the calculations. On the other hand, the MCA setup shows a noticeably smaller value in the measured throughput than in the calculated throughput. It seems that the spatial energy dispersion and resulting complicated beam profile not only affect the spectrometer resolution but also the spectrometer throughputs.

5. Summary and outlook

A collimation-based analyzer system for a RIXS spectrometer, dubbed SXC-RIXS, was designed and implemented to
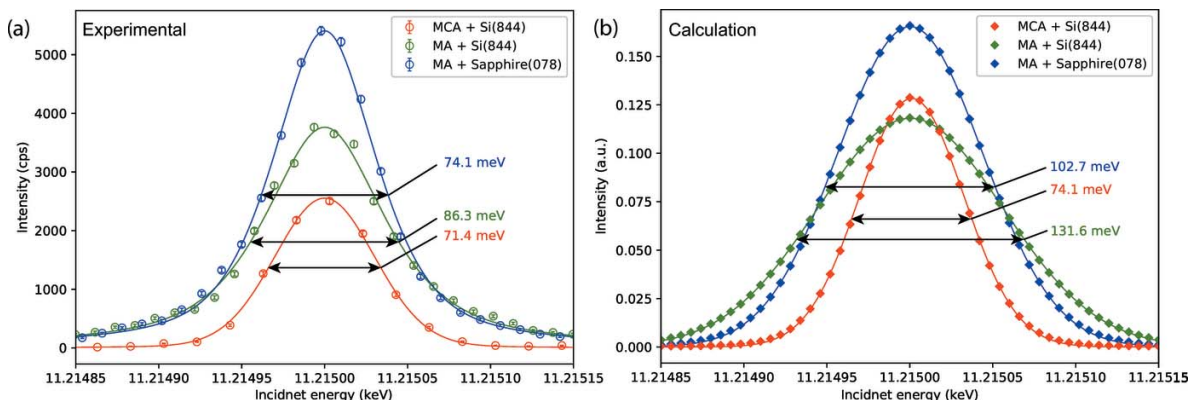
Figure 5
(a) Measured and (b) calculated incident-energy-dependence curves and their pseudo-Voigt fits (solid lines) for three different spectrometers. The full width at half-maximum (FWHM) of them correspond to the energy resolutions of the spectrometers. 3M Magic Scotch tape is used for an elastic reference scatterer for the experimental results.

Table 1
Measured and calculated FWHM energy resolutions and throughputs for three different spectrometers.

Throughputs are normalized to the values for 'MA + Sapph(078)'. All measured curves were fitted using a pseudo-Voigt function.

Spectrometer	Measured resolution (meV)	Calculated resolution (meV)	Measured throughput	Calculated throughput
MCA + Si(844)	71.4	74.1	0.4	0.54
MA + Si(844)	86.3	131.6	0.84	0.91
MA + Sapph(078)	74.1	102.7	1.00	1.00

study low-energy excitation spectra of samples under high pressure. In contrast to conventional spectrometers with diced spherical analyzers, this new setup can effectively remove extrinsic signals from a high-pressure sample environment and provide clean low-energy excitation spectra, thanks to the confocal nature of its first collimating element, a multilayer Montel mirror. Even in the extreme case when the applied pressure on the diamond anvil cell collapses the Be gasket into the sample, the SXC-RIXS spectrometer still provides a clean low-energy excitation, albeit with an increased elastic line. Experimental comparison of the energy resolutions of three different SCX-RIXS reveals that the MA and MCA setups give similar resolutions when using a medium-energy bandpass monochromator (70 meV), although the calculation claims that the MA setup would have worse resolutions. We attribute this discrepancy to the spatially energy-dispersed beam known to result from a monochromator based on asymmetrical crystals. Finally, an eventual SXC-RIXS type spectrometer is ideally suited to fulfill increasing demands for high-resolution RIXS measurements at high pressures, especially after the planned APS upgrade (APS-U).

APPENDIX A
Calculating A-crystal rocking curves and incident energy curves

The dynamical theory of diffraction was used to calculate incident energy curves (Authier, 2006). Multiplying the reflectivity of an analyzer and a double-Gaussian-shaped, which is assumed, exit beam from the Montel [Fig. 6(a)] gave the intensity curvature of the reflected beam from an analyzer [Fig. 6(b)]. One more identical step of multiplying reflectivity is added when a C-crystal is included. The volume under the curvature corresponds to the total intensity of the reflected beam after the analyzer. Incident energy dependence curves in Fig. 5(b) were acquired by changing an energy-centered position of the incident beam.

APPENDIX B
Effects of the spatial energy dispersion

As mentioned in the discussion section, the spatial energy dispersion generated by the asymmetrical monochromator could lead to better energy resolutions of the MA than that expected from calculations. We will explain how this could lead to better energy resolutions more specifically. Fig. 7(a)
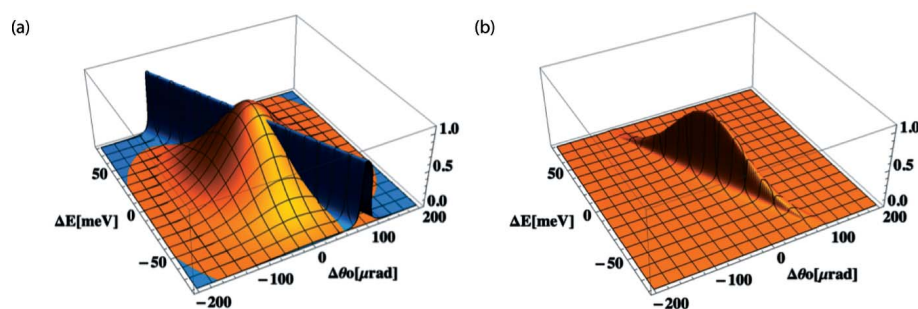

Figure 6
(a) Curvatures of a reflected beam from the Montel mirror (orange) and the acceptance of a flat crystal (blue). The reflected beam from the Montel mirror is assumed to be double-Gaussian and the acceptance is calculated by the dynamical diffraction theory. (b) Multiplying two curvatures in (a) of which the volumes under the surfaces give the intensity of the configuration.
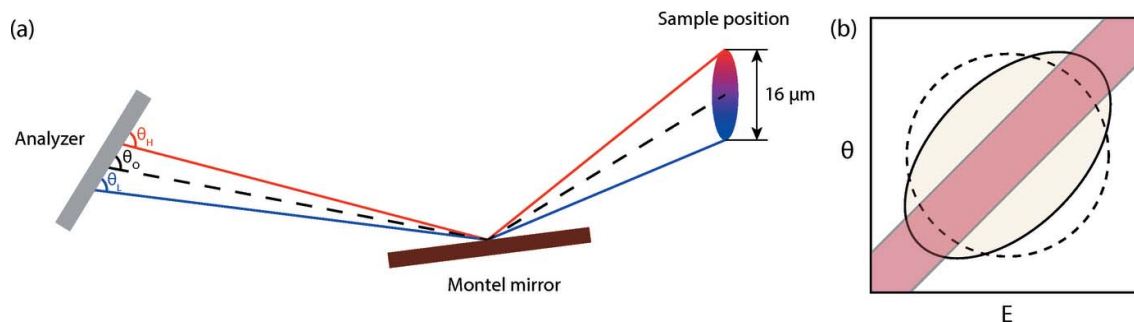
Figure 7
(*a*) Schematic of the MA setup used in the experiments. A spatial energy dispersion is expressed as gradation from red to blue at the sample position, and it is assumed that the energy is uniformly distributed along the whole vertical beam size of ∼16 μm. Thus, the top ray (red) has 35 meV higher energy than that of the center ray (dashed black). Due to a large acceptance of the Montel mirror, it reflects all rays to the analyzer. However, these reflected rays cannot be reflected by an analyzer at once since an analyzer usually has a small acceptance. (*b*) Conceptual Dumond diagram for a spatially energy-dispersed beam (ellipse) and a crystal reflectivity curve (red area). A spatial energy dispersion manifests as a diagonally shrunk ellipse from a perfect circle, which is for the case of a non-dispersed beam.

shows that the energy-dispersed beam was focused on the sample position with a finite beam size (∼16 μm). To simplify the case, we assume that energies are uniformly distributed in the vertical direction. The energy of the top ray (red) is 35 meV higher than that of the center ray (dashed black) and 70 meV higher than that of the bottom ray (blue). Then, the angle difference between the top (or bottom) ray and the center ray is roughly $\theta_H - \theta_0 = \theta_0 - \theta_L = \delta\theta \simeq (s/2)/\mathrm{WD}$, where s is the vertical beam size, and WD is the distance between the sample position and the Montel mirror. With $s = 16$ μm and WD = 200 mm, the angle difference $\delta\theta$ is about 40 μrad. Due to the large acceptance of the Montel mirror, all the scattered rays from the sample will be reflected to the analyzer. However, in the MA setup used in the experiments, the top (bottom) ray is incident on the analyzer with a larger (smaller) angle than the reference angle whereas it has higher energy (lower energy) or smaller (larger) Bragg angle than that of the reference ray. This effect can be described by a diagonally shrunk profile of the incident beam in a DuMond diagram as seen in Fig. 7(*b*). As the profile of the incident beam is shrunk along the reflectivity curve of the analyzer crystal, the energy resolution curve will be narrower than the non-dispersive case (dashed black circle). However, the energy resolutions are not easy to estimate without a real calculation because they are evaluated by a convolution of two complex and anisotropic two-dimensional curves. Still, we could see that this effect is more drastic when using Si(844) as an analyzer (34% reduction in resolution) than when using Sapph(078) (28% reduction), since it has smaller acceptance than that of Sapph(078) with a similar energy window at the Ir L_3-edge (Table 2), and is consequently more susceptible to this effect.

Funding information

Table 2
Parameters for the analyzer crystals.

Includes their Bragg angles, Darwin width and energy resolution at the Ir L_3-edge. All analyzer crystals are symmetric.

Crystal(orientation)	θ_B (°)	Width (μrad)	ΔE (meV)
Si(844)	85.73	17.4	14.57
Sapph(078)	87.22	28.6	15.58

References

Ament, L. J., Ghiringhelli, G., Sala, M. M., Braicovich, L. & van den Brink, J. (2009). *Phys. Rev. Lett.* **103**, 117003.

Ament, L. J. P., van Veenendaal, M., Devereaux, T. P., Hill, J. P. & van den Brink, J. (2011). *Rev. Mod. Phys.* **83**, 705–767.

Authier, A. (2006). *International Tables for Crystallography*, Vol. B, *Reciprocal Space*, edited by U. Shmueli, pp. 626–646. International Union of Crystallography.

Braicovich, L., van den Brink, J., Bisogni, V., Sala, M. M., Ament, L. J., Brookes, N. B., De Luca, G. M., Salluzzo, M., Schmitt, T., Strocov, V. N. & Ghiringhelli, G. (2010). *Phys. Rev. Lett.* **104**, 077002.

Haskel, D., Fabbris, G., Kim, J. H., Veiga, L. S. I., Mardegan, J. R. L., Escanhoela, C. A., Chikara, S., Struzhkin, V., Senthil, T., Kim, B. J., Cao, G. & Kim, J. W. (2020). *Phys. Rev. Lett.* **124**, 067201.

Haskel, D., Fabbris, G., Zhernenkov, M., Kong, P. P., Jin, C. Q., Cao, G. & van Veenendaal, M. (2012). *Phys. Rev. Lett.* **109**, 027204.

Heald, S., Seidler, G. T., Mortensen, D., Mattern, B., Bradley, J. A., Hess, N. & Bowden, M. (2012). *Proc. SPIE*, **8502**, 85020I.

Huang, X. R., Macrander, A. T., Honnicke, M. G., Cai, Y. Q. & Fernandez, P. (2012). *J. Appl. Cryst.* **45**, 255–262.

Huotari, S., Pylkkänen, T., Verbeni, R., Monaco, G. & Hämäläinen, K. (2011). *Nat. Mater.* **10**, 489–493.

Hwan Chun, S., Kim, J.-W., Kim, J., Zheng, H., Stoumpos, C., Malliakas, C., Mitchell, J., Mehlawat, K., Singh, Y., Choi, Y., Gog, T., Al-Zein, A., Sala, M., Krisch, M., Chaloupka, J., Jackeli, G., Khaliullin, G. & Kim, B. J. (2015). *Nat. Phys.* **11**, 462–466.

Kim, J. (2016). *High. Press. Res.* **36**, 391–403.

Kim, J., Casa, D., Said, A., Krakora, R., Kim, B. J., Kasman, E., Huang, X. & Gog, T. (2018). *Sci. Rep.* **8**, 1958.

Kim, J., Casa, D., Upton, M. H., Gog, T., Kim, Y. J., Mitchell, J. F., van Veenendaal, M., Daghofer, M., van den Brink, J., Khaliullin, G. & Kim, B. J. (2012). *Phys. Rev. Lett.* **108**, 177003.

Kim, J., Said, A. H., Casa, D., Upton, M. H., Gog, T., Daghofer, M., Jackeli, G., van den Brink, J., Khaliullin, G. & Kim, B. J. (2012). *Phys. Rev. Lett.* **109**, 157402.

Kim, J., Shi, X., Casa, D., Qian, J., Huang, X. & Gog, T. (2016). *J. Synchrotron Rad.* **23**, 880–886.

Li, B., Ji, C., Yang, W., Wang, J., Yang, K., Xu, R., Liu, W., Cai, Z., Chen, J. & Mao, H. K. (2018). *Proc. Natl Acad. Sci. USA*, **115**, 1713–1717.

Majumder, M., Manna, R. S., Simutis, G., Orain, J. C., Dey, T., Freund, F., Jesche, A., Khasanov, R., Biswas, P. K., Bykova, E., Dubrovinskaia, N., Dubrovinsky, L. S., Yadav, R., Hozoi, L., Nishimoto, S., Tsirlin, A. A. & Gegenwart, P. (2018). *Phys. Rev. Lett.* **120**, 237202.

Mundboth, K., Sutter, J., Laundy, D., Collins, S., Stoupin, S. & Shvyd'ko, Y. (2014). *J. Synchrotron Rad.* **21**, 16–23.

Rossi, M., Henriquet, C., Jacobs, J., Donnerer, C., Boseggia, S., Al-Zein, A., Fumagalli, R., Yao, Y., Vale, J. G., Hunter, E. C., Perry, R. S., Kantor, I., Garbarino, G., Crichton, W., Monaco, G., McMorrow, D. F., Krisch, M. & Moretti Sala, M. (2019). *J. Synchrotron Rad.* **26**, 1725–1732.

Shvyd'ko, Y., Stoupin, S., Shu, D., Collins, S. P., Mundboth, K., Sutter, J. & Tolkiehn, M. (2014). *Nat. Commun.* **5**, 4219.

Shvyd'ko, Y. V., Hill, J. P., Burns, C. A., Coburn, D. S., Brajuskovic, B., Casa, D., Goetze, K., Gog, T., Khachatryan, R., Kim, J. H., Kodituwakku, C. N., Ramanathan, M., Roberts, T., Said, A., Sinn, H., Shu, D., Stoupin, S., Upton, M., Wieczorek, M. & Yavas, H. (2013). *J. Electron Spectrosc. Relat. Phenom.* **188**, 140–149.

Yadav, R., Rachel, S., Hozoi, L., van den Brink, J. & Jackeli, G. (2018). *Phys. Rev. B*, **98**, 121107(R).